PAPER

WILEY | Terra Nova

Environmental controls on [10]Be-based catchment-averaged denudation rates along the western margin of the Peruvian Andes

Regina Reber[1] 🔾 | Romain Delunel[1] | Fritz Schlunegger[1] | Camille Litty[1] | Andrea Madella[1] | Naki Akçar[1] | Marcus Christl[2]

[1]Institute of Geological Sciences, University of Bern, Bern, Switzerland

[2]Laboratory of Ion Beam Physics (LIP), ETH Zürich, Zürich, Switzerland

Correspondence
Regina Reber, Institute of Geological Sciences, University of Bern, Bern, Switzerland.
Email: rreber@geo.unibe.ch

Abstract

We present [10]Be-based basin-averaged denudation rates for the entire western margin of the Peruvian Andes. Denudation rates range from *c.* 9 mm ka^{-1} to 190 mm ka^{-1} and are related neither to the subduction of the Nazca plate nor to the current seismicity along the Pacific coast and the occurrence of raised Quaternary marine terraces. Therefore, we exclude a tectonic control on denudation on a millennial time-scale. Instead, we explain >60% of the observed denudation rates with a model where erosion rates increase either with mean basin slope angles or with mean annual water discharge. These relationships suggest a strong environmental control on denudation.

1 | INTRODUCTION

The western margin of the Peruvian Andes is considered to be a prime example of a plate boundary where the oceanic Nazca plate has been subducting beneath the continental South American plate since at least Jurassic times (Isacks, 1988). Because of active subduction, the Peruvian Andes have experienced frequent and strong earthquakes during their geologic history and still do nowadays (Nocquet et al., 2014). Therefore, it is not surprising that erosion along the western Andean margin has been considered to depend strongly on the occurrence of earthquakes. This interpretation was proposed by McPhillips, Bierman, and Rood (2014) based on [10]Be concentrations measured in pebbles in the Pisco valley, 13°S latitude. Contrariwise, Abbühl et al. (2011) reported positive correlations between mean annual precipitation, basin morphometry and [10]Be-based catchment-averaged denudation for three basins situated on the western Andean margin, between 5°S and 20°S latitude, thus pointing to an environmental control on denudation. However, because [10]Be-based investigations have been conducted at a few sites only, interpretations about the primary controls on denudation have remained non-conclusive (Abbühl et al.,

2011; Bekaddour et al., 2014; McPhillips et al., 2014). Here, we re-address this problem based on a dataset where we measured [10]Be-based denudation rates for all >700 km^2 basins along the entire western margin of the Peruvian Andes. We collected stream-sediment samples from 42 streams (Figure 1) and analysed their concentrations of in situ produced cosmogenic [10]Be, based on which we inferred basin-averaged denudation rates. We then explored possible correlations between the denudation rate pattern, the basin's morphometric properties, the stream's mean annual runoff and the seismotectonic situation of the region. The scope is to explore whether denudation in this part of the Andes can best be explained by environmental conditions or rather reflects a response to the subduction processes and the related seismicity and uplift pattern.

2 | SETTING

The western margin of northern South America has evolved through the subduction of the Farallón-Nazca oceanic plate beneath the South American continental plate and the accretion

FIGURE 1 Map of the western margin of the Peruvian Andes showing drainage basins that were sampled for [10]Be-based denudation rates, patterns of quartz contents of the underlying bedrock, which were estimated from the geological map of Peru and northern Chile (INGEMMET, 2011; SERNAGEOMIN, 2004) plus assignments of quartz contents for these lithologies (Carretier et al., 2015), and contour lines of mean annual precipitation rates. The map also shows the major Peruvian cities. The inset shows a general overview of the atmospheric circulation pattern around the Intertropical Convergence Zone, ITCZ of South America [Colour figure can be viewed at wileyonlinelibrary.com]
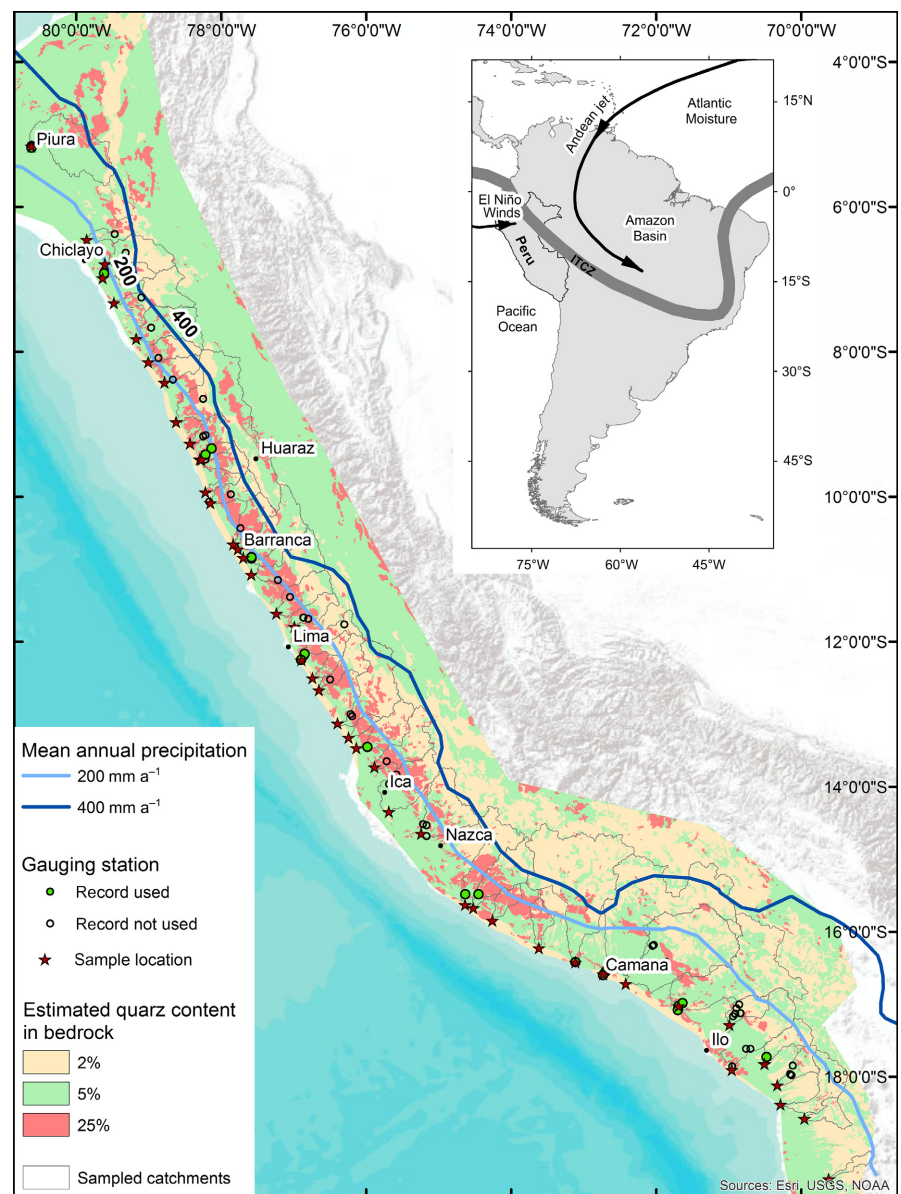
of crustal blocks since at least Early Jurassic times (e.g., Isacks, 1988). The Western Escarpment, the focus of this study, is a gently folded ramp, connecting the western margin of the Meseta and the Altiplano in northern and southern Peru, respectively, with the Pacific Ocean. It is composed of Late Oligo/Miocene fluvio-volcanoclastic deposits near the Pacific coast that are underlain by Mesozoic tholeiitic arc rocks, marine backarc sediments (Vidal, 1993) and the Cretaceous Coastal Batholith, a suite of granitic to dioritic rocks with varying quartz contents (Figure 1). The shortening and thickening of the Andes was associated with the topographic rise of the Altiplano Plateau to its current elevation (Barnes & Ehlers, 2009). The topographic rise also resulted in a change in atmospheric circulation and precipitation patterns, and river incision (Schildgen, Hodges, Whipple, Reiners, & Pringle, 2007; Thouret et al., 2007). The morphology of the Western Escarpment can be characterized as a steep ramp, which was formed through uplift during the Miocene (Schildgen et al., 2007).

Upstream of this ramp on the Meseta/Altiplano (>3,000 m a.s.l.) streams have remained graded to a Late Miocene base level constituted by a series of Tertiary volcanic-volcanoclastic rocks, thereby forming a cap rock (Abbühl et al., 2011). Within the ramp, streams have deeply incised into Mesozoic plutonic and metasedimentary rocks via a series of steep, headward-retreating knickzones that grade to the present-day base level defined by the Pacific Ocean (Schildgen et al., 2007).

Strong N–S and E–W precipitation gradients and seasonality in the western Andes are related to the positions of the Andean jet and the Intertropical Convergence Zone, ITCZ (Garreaud, Vuille, & Clement, 2003; inset of Figure 1). On the western margin of the High Andes, precipitation rates decrease from ~1000 mm a^{-1} near the Equator to <200 mm a^{-1} in northern Chile. During austral summer, the ITCZ is at its southernmost extent near the border between Peru and Bolivia, transferring humidity from the tropical Amazon basin and the Atlantic to the Altiplano (Garreaud et al., 2003). During austral winter, the

TABLE 1 Morphometric dataset for the sampled drainage basins. All calculations are based on the 90-m resolution DEM (SRTM; Jarvis et al., 2008). Cosmogenic data from the Lluta basin are taken from Kober et al. (2009), while Abbühl et al. (2010, 2011) presented [10]Be concentrations for the Piura and Pisco basins

Sample name/ catchment name	Latitude, °N sample location (DD.DD) WGS84	Longitude, °E sample location (DD.DD) WGS84	Latitude, °N centroid catchment polygon (DD.DD) WGS84	Drainage area (km²)	Shielding factor	Mean elevation (m a.s.l.)	Mean slope (m m⁻¹)	Hypsometric integral HI
PRCME-1	−18.1191	−70.3274	−17.8424	1659	0.9832	2,733	0.28	0.45
PRCME-3	−17.8240	−70.5046	−17.4844	2154	0.9826	3,105	0.30	0.50
PRCME-401	−17.9073	−70.9562	−17.3244	5821	0.9913	2,668	0.19	0.46
PRCME-5	−17.2865	−70.9895	−17.0601	1785	0.9873	3,398	0.26	0.52
PRCME-6	−17.0288	−71.6908	−16.5526	13026	0.9860	3,568	0.24	0.63
PRCME-7	−16.5849	−72.7285	−15.6579	17557	0.9851	3,635	0.23	0.57
PRCME-8	−16.7192	−72.4187	−16.2168	13862	0.9940	3,285	0.15	0.52
PRCME-9	−16.4217	−73.1153	−15.2406	16065	0.9793	3,745	0.26	0.59
PRCME-10	−16.2260	−73.6178	−15.8353	1420	0.9886	2,155	0.23	0.56
PRCME-11	−15.8460	−74.2607	−15.5630	1244	0.9787	2,316	0.34	0.50
PRCME-12	−15.6720	−74.5232	−15.1800	4361	0.9812	2,797	0.28	0.54
PRCME-13	−15.6286	−74.6368	−14.8915	4561	0.9840	2,895	0.26	0.61
PRCME-1401	−14.6476	−75.2424	−14.2938	5220	0.9806	2,716	0.32	0.57
PRCME-15	−14.3448	−75.6858	−13.9437	4715	0.9846	2,204	0.26	0.44
PRCME-17	−13.4650	−76.1365	−13.1879	3113	0.9706	3,197	0.37	0.60
PRCME-18	−13.3213	−76.2433	−13.1391	726	0.9813	1,967	0.33	0.44
PRCME-19	−13.1238	−76.3944	−12.5965	6059	0.9641	3,648	0.40	0.62
PRCME-20	−12.6652	−76.6515	−12.3399	2,337	0.9650	3,294	0.41	0.57
PRCME-21	−12.5005	−76.7412	−12.2700	715	0.9746	1,772	0.36	0.42
PRCME-22	−12.2510	−76.8919	−12.0626	1,574	0.9710	2,568	0.38	0.48
PRCME-23	−11.6083	−77.2387	−11.3225	3,070	0.9694	2,697	0.39	0.51
PRCME-24	−11.0713	−77.5860	−10.9196	4,322	0.9625	3,134	0.42	0.56
PRCME-25	−10.8390	−77.6962	−10.8311	1,013	0.9707	2,365	0.38	0.45
PRCME-26	−10.6551	−77.8337	−10.2753	2,365	0.9701	2,407	0.39	0.49
PRCME-27	−8.9662	−78.6209	−8.8916	12,385	0.9663	3,262	0.38	0.48
PRCME-28	−8.4230	−78.7835	−8.2126	1,695	0.9802	2,246	0.31	0.52
PRCME-29	−8.1400	−79.0076	−7.9708	2,120	0.9784	2,307	0.32	0.53
PRCME-30	−7.3234	−79.4807	−7.1779	3,901	0.9747	2,292	0.34	0.54
PRCME-31	−6.9804	−79.6335	−6.8922	1,755	0.9840	1,142	0.24	0.28
PRCME-32	−6.4519	−79.8572	−6.3479	1,378	0.9794	1,423	0.28	0.34
PRCME-33	−6.7882	−79.6043	−6.6466	3,552	0.9805	1,844	0.30	0.44
PRCME-34	−7.8193	−79.1728	−7.6299	4,363	0.9655	1,985	0.40	0.43
PRCME-35	−9.2627	−78.4313	−9.0937	1,777	0.9676	2,194	0.39	0.42
PRCME-36	−9.4815	−78.2945	−9.3510	750	0.9683	1,938	0.38	0.38
PRCME-3601	−9.4861	−78.2737	−9.5140	1,816	0.9677	2,595	0.40	0.53
PRCME-37	−9.9359	−78.2186	−9.7839	685	0.9697	1,697	0.37	0.36
PRCME-38	−10.0847	−78.1504	−9.9086	2,100	0.9723	2,337	0.37	0.47
PRCME-39	−11.7923	−76.9914	−11.5598	1,764	0.9692	2,942	0.39	0.52
PAT-ME	−10.7203	−77.7695	−10.4022	4,607	0.9545	3,378	0.44	0.52
LIM-ME	−11.9175	−76.6199	−11.8094	1,207	0.9545	3,936	0.47	0.63
Lluta LLT3	−18.3833	−70.2833	−18.1032	3,322	0.9890	3,533	0.21	0.58
Piura Piu2	−5.1619	−80.6161	−5.1874	7,515	0.9875	632	0.19	0.17

(Continues)

TABLE 1 (Continued)

Sample name/ catchment name	Latitude, °N sample location (DD.DD) WGS84	Longitude, °E sample location (DD.DD) WGS84	Latitude, °N centroid catchment polygon (DD.DD) WGS84	Drainage area (km²)	Shielding factor	Mean elevation (m a.s.l.)	Mean slope (m m⁻¹)	Hypsometric integral HI
Pisco TRU13	−13.7274	−75.8855	−13.3852	3,667	0.9753	3,464	0.34	0.63
AZCE	−18.5803	−69.9543	−18.5149	1,434	0.9858	3,306	0.25	0.56
FRCE	−19.4121	−69.6192	−19.1976	661	0.9914	3,801	0.21	0.57

TABLE 2 Information relevant for interpreting ^{10}Be concentrations. Note that we have used the denudation rates corrected for various quartz contents (indicated in bold) to illustrate the relationships in Figure 4. Catchment-averaged denudation rates were calculated using the CAIRN method developed by Mudd et al. (2016) using the SRTM DEM that we up-scaled to a 200-m resolution for computing efficiency purposes. Calculations were accomplished using the default parameters in CAIRN, which include a ^{10}Be half-life of 1.39 ± 0.01 Ma (Chmeleff et al., 2010; Korschinek et al., 2010) and a SLHL ^{10}Be production rate of 4.30 at.g⁻¹.a⁻¹ (Braucher, Merchel, Borgomano, & Bourlès, 2011) and consider the neutrons, fast and slow muons attenuation lengths and contribution following Braucher et al. (2011). We used a rock density of 2.65 g cm⁻³. Please note that Carretier et al. (2015) reported similar denudation rates for the Ocoña basin

Sample name	Quartz dissolved (g)	^{9}Be spike (mg)	Measured ^{10}Be/^{9}Be ratio (10⁻¹²)	AMS error (%)	^{10}Be concentration (10⁴ at. g⁻¹)	Denudation rates (mm ka⁻¹)	Denudation rate, corrected for Qz content in bedrock (mm ka⁻¹)
PRCME-1	40.0348	0.2000	3.06	2	101.9 ± 2.2	13.3 ± 3.6	**12.2 ± 3.3**
PRCME-3	39.3835	0.1732	1.89	3	55.6 ± 1.4	28.6 ± 5.3	**27.7 ± 5.2**
PRCME-401	40.8110	0.1998	2.78	2	91.0 ± 1.8	15.2 ± 3.9	**12.5 ± 3.2**
PRCME-5	39.7310	0.2021	2.46	2	83.4 ± 1.9	21.4 ± 4.8	**18.6 ± 4.1**
PRCME-6	37.2702	0.1722	0.71	4	21.9 ± 0.8	89.7 ± 16.7	**72.1 ± 13.4**
PRCME-7	39.8668	0.2009	0.47	3	15.7 ± 0.4	127.5 ± 23.4	**106.8 ± 19.6**
PRCME-8	38.6178	0.2002	1.47	4	50.8 ± 2.0	34.0 ± 6.4	**27.7 ± 5.2**
PRCME-9	40.8767	0.2002	0.26	4	8.5 ± 0.4	242.1 ± 45.0	**184.1 ± 34.2**
PRCME-10	41.0053	0.2022	2.84	2	93.6 ± 1.9	8.7 ± 1.7	**9.6 ± 1.9**
PRCME-11	40.1231	0.2003	1.98	2	65.9 ± 1.6	14.7 ± 2.9	**15.2 ± 2.9**
PRCME-12	41.8460	0.1984	1.89	2	59.6 ± 1.2	21.2 ± 4.0	**15.3 ± 2.9**
PRCME-13	35.5703	0.1736	0.66	4	21.3 ± 0.8	66.5 ± 12.6	**40.6 ± 7.7**
PRCME-1401	40.1839	0.2022	0.81	3	27.3 ± 0.8	46.1 ± 8.6	**29.4 ± 5.5**
PRCME-15	39.5359	0.1998	1.09	3	36.6 ± 1.0	27.0 ± 5.7	**25.1 ± 5.3**
PRCME-17	38.1530	0.1997	0.52	3	18.1 ± 0.5	61.2 ± 11.7	**44.1 ± 8.4**
PRCME-18	40.2356	0.2004	1.07	2	35.4 ± 0.8	32.9 ± 6.2	**27.5 ± 5.2**
PRCME-19	25.7694	0.1738	0.64	4	28.8 ± 1.1	66.8 ± 12.3	**51.2 ± 9.5**
PRCME-20	24.8438	0.1909	0.51	3	26.1 ± 0.8	27.1 ± 5.4	**17.9 ± 3.6**
PRCME-21	41.3246	0.2019	0.80	3	26.2 ± 0.8	25.9 ± 5.2	**21.6 ± 4.4**
PRCME-22	39.9407	0.2018	0.91	2	30.6 ± 0.6	38.5 ± 7.1	**23.6 ± 4.4**
PRCME-23	45.3875	0.2005	0.48	4	14.1 ± 0.5	97.7 ± 18.4	**52.8 ± 10.0**
PRCME-24	40.1698	0.2008	0.34	3	11.3 ± 0.4	137.1 ± 25.6	**82.5 ± 15.4**
PRCME-25	40.3298	0.1967	0.78	2	25.4 ± 0.6	41.7 ± 7.7	**25.6 ± 4.7**
PRCME-26	41.3739	0.2031	0.97	3	31.7 ± 0.9	32.5 ± 6.5	**19.6 ± 3.9**
PRCME-27	40.0497	0.1992	0.68	4	22.6 ± 0.9	71.2 ± 13.4	**70.4 ± 13.2**
PRCME-28	10.8368	0.1755	0.58	4	62.0 ± 2.6	14.9 ± 3.0	**9.1 ± 1.8**
PRCME-29	41.8022	0.2017	1.33	3	42.7 ± 1.4	22.0 ± 5.0	**12.9 ± 2.9**
PRCME-30	39.6707	0.2008	0.89	3	29.9 ± 0.9	30.5 ± 5.9	**25.8 ± 5.0**
PRCME-31	37.3769	0.2011	0.99	3	35.4 ± 1.0	14.1 ± 3.0	**10.0 ± 2.1**
PRCME-32	40.0900	0.1973	0.80	2	26.2 ± 0.6	20.1 ± 4.2	**20.8 ± 4.4**

TABLE 2 (Continued)

Sample name	Quartz dissolved (g)	^{9}Be spike (mg)	Measured ^{10}Be/^{9}Be ratio (10^{-12})	AMS error (%)	^{10}Be concentration (10^4 at. g^{-1})	Denudation rates (mm ka^{-1})	Denudation rate, corrected for Qz content in bedrock (mm ka^{-1})
PRCME-33	40.8828	0.2003	0.69	3	22.4 ± 0.7	32.5 ± 6.5	**25.2 ± 5.1**
PRCME-34	40.2766	0.2006	0.44	3	14.4 ± 0.4	50.1 ± 9.2	**45.7 ± 8.4**
PRCME-35	40.5293	0.1985	0.51	3	16.7 ± 0.4	64.9 ± 12.4	**45.9 ± 8.8**
PRCME-36	39.6159	0.2003	0.65	3	21.9 ± 0.7	54.3 ± 10.3	**43.0 ± 8.2**
PRCME-3601	40.0750	0.2009	0.55	3	18.2 ± 0.6	65.6 ± 12.5	**38.2 ± 7.3**
PRCME-37	39.9118	0.1997	0.62	4	20.8 ± 0.8	35.3 ± 7.1	**21.3 ± 4.3**
PRCME-38	28.0939	0.1912	1.16	2	52.8 ± 1.1	19.7 ± 4.5	**10.1 ± 2.3**
PRCME-39	40.5531	0.1989	0.52	3	17.0 ± 0.6	82.2 ± 15.5	**53.4 ± 10.1**
PAT-ME	50.1067	0.1991	0.24	4	6.4 ± 0.3	260.1 ± 48.8	**190.9 ± 35.8**
LIM-ME	50.1962	0.1994	0.40	12	10.5 ± 1.3	197.6 ± 43.3	**151.7 ± 33.2**
Lluta LLT3	–	–	–	–	86.6 ± 5.4	22.1 ± 4.3	**20.1 ± 3.9**
Piura Piu2	–	–	–	–	19.1 ± 0.0	16.9 ± 4.2	**20.4 ± 5.0**
Pisco TRU13	–	–	–	–	17.1 ± 1.2	104.1 ± 20.4	**69.1 ± 13.5**
AZCE	52.78	0.17	3.69	2	80.3 ± 1.5	20.2 ± 3.8	**19.1 ± 3.6**
FRCE	17.21	0.17	0.91	2	61.3 ± 1.5	35.0 ± 6.8	**32.4 ± 6.3**

subtropical jet stream and the ITCZ are located close to the Equator, resulting in persistently dry conditions on the plateau.

3 | SAMPLING STRATEGY, DENUDATION-RATE CALCULATIONS AND COMPARISONS WITH MORPHOMETRIC PARAMETERS

We collected 42 stream-sediment samples along the Pacific coast between 6°S and 20°S latitudes for analyses of in situ ^{10}Be concentrations in detrital quartz (Figure 1, Table 1). Basins associated with the samples have drainage areas that are >700 km^2. In situ ^{10}Be concentrations of quartz, extracted from stream sediments of the Piura River in northern Peru (Abbühl et al., 2010), the Pisco River (Abbühl et al., 2011) and the Lluta River in northern Chile (Kober et al., 2009) were also considered (Table 1). All samples were processed for accelerator mass spectrometry measurements using the protocols of Akçar et al. (2012). The measured ^{10}Be/^{9}Be ratios were normalized to ETH in-house standard S2007N (Kubik & Christl, 2010) based on the ^{10}Be half-life of 1.39 ± 0.01 Ma (Chmeleff et al., 2010; Korschinek et al., 2010). Reported ^{10}Be concentrations are corrected for procedural blanks; associated 1-sigma uncertainties include analytical counting errors on standard, blank and sample measurements (Table 2). The catchment-averaged denudation rates reported in Table 2 were computed using the numerical solutions provided by Mudd, Harel, Hurst, Grieve, and Marrero (2016), in which production and shielding for in situ ^{10}Be are calculated on a pixel-by-pixel basis. We did not consider snow cover to have a major impact on the results as the mean basin elevations of the sampled catchments are largely situated below the snow line, and, therefore, we excluded it from calculations. Spatially variable quartz contents of the source-rock lithologies can add a

bias in the determinations of basin-averaged denudation rates (Carretier et al., 2015). We considered this issue by categorizing the bedrock of the sampled basins according to the litho-tectonic architecture of the underlying bedrock (geological map 1:1,000,000 of Peru and Chile; INGEMMET, 2011, SERNAGEOMIN, 2004). Following Carretier et al. (2015), we assigned relative abundances of quartz contents: 25% for plutonic rocks, 5% for Mesozoic to Quaternary sedimentary rocks and 2% for the remaining lithotypes (e.g., volcanoclastic rocks). As will be shown later, this correction generally yields lower denudation-rate estimates, but does not affect their spatial pattern.

Catchment-scale morphometric parameters and characteristics (Table 1), including drainage area, mean elevation, slope angle, hypsometry and latitude, were extracted from the 90-m resolution digital elevation model Shuttle Radar Topography Mission (SRTM; Jarvis, Reuter, Nelson, & Guevara, 2008). The mean annual water discharge (Table 3) was obtained by combining hydrological data reported by the Sistema Nacional de Información de Recursos Hídricos and the TRMM-V6.3B43.2 precipitation database (Huffman et al., 2007). Averaged gauging station records were plotted as a function of theoretical runoff, estimated as the product of contributing area and TRMM-based precipitation rate, for a selection of 12 basins for which hydrological stations and river-sediment sampling sites were separated by less than 5 km (Figure 1). The observed 60% water budget loss, possibly due to evaporation and irrigation, was then used to estimate a TRMM-based runoff for the other basins, where hydrological stations were far from sampling sites. Possible co-variations and correlations between denudation rates and/or morphometric parameters and basin characteristics were evaluated using Pearson correlation coefficients, thus providing corresponding *p*-values with a significance level alpha of 0.05 (Table 4).

TABLE 3 Hydrological dataset including information about gauging stations, related records and TRMM-based precipitation rates. The precipitation data are derived from the medium-resolution (c. 25 × 25 km) rainfall dataset TRMM V6.3B43.2 (Huffman et al., 2007) averaged over 12 years from 1998 to 2010. We resampled this dataset to a 1 × 1 km grid in order to ensure adequate coverage for each drainage basin. The estimated runoff is extracted and computed from this precipitation data. Number of the national gauging station used for averaging an annual runoff. These latter data are taken from the SNIRH (Sistema Nacional de Información de Recursos Hídricos); http://snirh.ana.gob. pe/consultasSnirh/ConsHidrom2.aspx

Sample name	River name	Mean annual precipitation (mm a^{-1})	Mean annual water discharge (m^3 s^{-1})	Code of gauging station SNIRH	Years of observations for stations situated at <5-km distance from the ^{10}Be sampling sites	Number of available records
PRCME-1	Quebrada Arunta	149.6 ± 0.1	3.4	191311; 205201; 205202		
PRCME-3	Rio Sama	136.4 ± 0.1	4.0	**205103**	**1963-89/2000-04/2011-14**	339
PRCME-401	Rio Locumba	115.0 ± 0.1	9.2	205010; 191011; 00858		
PRCME-5	Rio Moquegua	137.8 ± 0.1	3.4	131721000(1/2/3/4); 204804; 204812		
PRCME-6	Rio Tambo	216.3 ± 0.1	38.1	**204108; 204905; 204903**	**1952-86/1995-2010/ 2011-16**	442
PRCME-7	Rio Camana	283.9 ± 0.1	68.4	**204614; 204621**	**1960-63/1971-86/2005-10 2014-16**	280
PRCME-8	Rio Quilca	170.2 ± 0.1	30.1	204706; 1322310001; 204714		
PRCME-9	Rio Ocona	414.7 ± 0.1	91.1	**204504**	**1970-73/1984/1986/ 2004-05/2007/2014**	64
PRCME-10	Rio Atico	141.3 ± 0.1	2.7	No station		
PRCME-11	Quebrada de Chala	166.6 ± 0.1	2.8	No station		
PRCME-12	Rio Yauca	313.1 ± 0.2	18.5	**204002**	**2014-2016**	23
PRCME-13	Rio Acari	318.4 ± 0.2	19.8	**203903**	**2014-2016**	25
PRCME-1401	Rio Grande	283.6 ± 0.1	20.4	203802; 203804; 203805		
PRCME-15	Rio Ica	188.4 ± 0.1	12.1	203702; 203703		
PRCME-17	Rio Chico	237.8 ± 0.1	10.1	**203501**	**1950-1990/2002/2008**	394
PRCME-18	Quebrada Topara	138.4 ± 0.2	1.3	No station		
PRCME-19	Rio Canete	318.4 ± 0.1	26.4	203302; 203301		
PRCME-20	Rio Mala	257.6 ± 0.2	8.2	203101		
PRCME-21	Quebrada Chilca	116.6 ± 0.1	1.1	No station		
PRCME-22	Rio Lurin	175.5 ± 0.2	3.7	**203005; 203006**	**1950-1961/1972-1984**	210
PRCME-23	Rio Chancay	211.4 ± 0.1	8.9	202701		
PRCME-24	Rio Huaura	316.9 ± 0.2	18.7	202609		
PRCME-25	Rio Supe	275.4 ± 0.3	3.8	**202501; 202502**	**1964-1973**	42
PRCME-26	Rio Fortaleza	355.4 ± 0.2	11.5	202301		
PRCME-27	Rio Santa	571.7 ± 0.2	96.1	211402		
PRCME-28	Rio Viru	330.9 ± 0.2	7.7	201501		
PRCME-29	Rio Moche	383.2 ± 0.2	11.0	201401		
PRCME-30	Rio Jequetepeque	472.8 ± 0.2	25.4	201204		
PRCME-31	Rio Zana	381.3 ± 0.2	9.1	**201003**	**1972-1976**	49
PRCME-32	Rio Motupe	297.9 ± 0.2	5.7	200801		
PRCME-33	Rio Reque	438.7 ± 0.2	21.3	200907		
PRCME-34	Rio Chicama	422.5 ± 0.2	24.7	201302; 201303		
PRCME-35	Rio Samanco	248.8 ± 0.2	6.0	201901; 201902		
PRCME-36	Rio Sechin	219.2 ± 0.3	2.2	**202003; 202005**	**1950/1957/1965/1967/ 1971-90**	135
PRCME-3601	Rio Casma	345.6 ± 0.3	8.6	202004		

(Continues)

TABLE 3 (Continued)

Sample name	River name	Mean annual precipitation (mm a^{-1})	Mean annual water discharge (m^3 s^{-1})	Code of gauging station SNIRH	Years of observations for stations situated at <5-km distance from the ^{10}Be sampling sites	Number of available records
PRCME-37	Rio Culebras	254.9 ± 0.3	2.4	No station		
PRCME-38	Rio Huarmey	340.1 ± 0.3	9.8	202201; 202202		
PRCME-39	Rio Chillon	204.7 ± 0.1	4.9	202804; 202806		
PAT-ME	Rio Pativilca	490.6 ± 0.2	30.9	202401; 202402		
LIM-ME	Rio Rimac	270.0 ± 0.1	4.4	202905		
Lluta LLT3	Rio Lluta	160.7 ± 0.1	7.3	No station		
Piura Piu2	Rio Piura	352.7 ± 0.0	36.6	**200426; 137812004; 200406**	1925-28/1975/1978-82/1984/1991-97/2014-16	158
Pisco TRU13	Rio Pisco	272.6 ± 0.1	13.6	203602		
AZCE	Rio Azapa	109.1 ± 0.1	2.1	No station		
FRCE	Rio Tiliviche	128.9 ± 0.2	1.2	No station		

TABLE 4 Results of the statistical investigations, illustrated here as a correlation matrix together with the p-values. Note that the slope and discharge do not show any obvious correlations and are thus independent variables. (a and b) Statistical results using denudation rates that have not been corrected for various quartz contents in bedrock; (c and d) same as before, but based on denudation rates that have been corrected for various quartz contents. See text for further details

Variables	Denudation	Discharge	Slope	Precipitation	Elevation	Drainage area	Latitude	HI
(a) Correlation matrix (Pearson)								
Denudation	**1**	**0.49**	**0.37**	**0.36**	**0.51**	**0.41**	0.01	**0.38**
Discharge	**0.49**	**1**	−0.13	**0.59**	0.29	**0.88**	0.07	0.13
Slope	**0.37**	−0.13	**1**	**0.33**	0.06	**−0.36**	**0.44**	0.14
Precipitation	**0.36**	**0.59**	**0.33**	**1**	−0.12	**0.30**	**0.69**	−0.08
Elevation	**0.51**	0.29	0.06	−0.12	**1**	**0.37**	**−0.64**	**0.86**
Drainage area	**0.41**	**0.88**	**−0.36**	**0.30**	**0.37**	**1**	−0.17	0.21
Latitude	0.01	0.07	**0.44**	**0.69**	**−0.64**	−0.17	**1**	**−0.54**
Hi	**0.38**	0.13	0.14	−0.08	**0.86**	0.21	**−0.54**	**1**
(b) p-values								
Denudation	**0**	**0.001**	**0.011**	**0.014**	**0.000**	**0.005**	0.963	**0.011**
Discharge	**0.001**	**0**	0.402	**<0.0001**	0.057	**<0.0001**	0.667	0.407
Slope	**0.011**	0.402	**0**	**0.025**	0.688	**0.015**	**0.002**	0.374
Precipitation	**0.014**	**<0.0001**	**0.025**	**0**	0.429	**0.046**	**<0.0001**	0.593
Elevation	**0.000**	0.057	0.688	0.429	**0**	**0.012**	**<0.0001**	**<0.0001**
Drainage area	**0.005**	**<0.0001**	**0.015**	**0.046**	**0.012**	**0**	0.271	0.174
Latitude	0.963	0.667	**0.002**	**<0.0001**	**<0.0001**	0.271	**0**	**0.000**
Hi	**0.011**	0.407	0.374	0.593	**<0.0001**	0.174	**0.000**	**0**
(c) Correlation matrix (Pearson)								
Denudation	**1**	**0.56**	**0.31**	**0.37**	**0.52**	**0.47**	−0.02	**0.35**
Discharge	**0.56**	**1**	−0.13	**0.59**	0.29	**0.88**	0.07	0.13
Slope	**0.31**	−0.13	**1**	**0.33**	0.06	**−0.36**	**0.44**	0.14
Precipitation	**0.37**	**0.59**	**0.33**	**1**	−0.12	**0.30**	**0.69**	−0.08
Elevation	**0.52**	0.29	0.06	−0.12	**1**	**0.37**	**−0.64**	**0.86**
Drainage area	**0.47**	**0.88**	**−0.36**	**0.30**	**0.37**	**1**	−0.17	0.21

(Continues)

TABLE 4 (Continued)

Variables	Denudation	Discharge	Slope	Precipitation	Elevation	Drainage area	Latitude	HI
Latitude	−0.02	0.07	**0.44**	**0.69**	**−0.64**	−0.17	**1**	**−0.54**
Hi	**0.35**	0.13	0.14	−0.08	**0.86**	0.21	**−0.54**	**1**
(d) *p*-values								
Denudation	**0**	**0.000**	**0.038**	**0.012**	**0.000**	**0.001**	0.910	**0.017**
Discharge	**<0.0001**	**0**	0.402	**<0.0001**	0.057	**<0.0001**	0.667	0.407
Slope	**0.038**	0.402	**0**	**0.025**	0.688	**0.015**	**0.002**	0.374
Precipitation	**0.012**	**<0.0001**	**0.025**	**0**	0.429	**0.046**	**<0.0001**	0.593
Elevation	**0.000**	0.057	0.688	0.429	**0**	**0.012**	**<0.0001**	**<0.0001**
Drainage area	**0.001**	**<0.0001**	**0.015**	**0.046**	**0.012**	**0**	0.271	0.174
Latitude	0.910	0.667	**0.002**	**<0.0001**	**<0.0001**	0.271	**0**	**0.000**
Hi	**0.017**	0.407	0.374	0.593	**<0.0001**	0.174	**0.000**	**0**

Values in bold are different from 0 with a significance level alpha = 0.05.

FIGURE 2 Patterns of [10]Be-based catchment-averaged denudation rates plus tectonic situation including the depth of the subducted slab (solid and dashed brown lines); slab depths, taken from earthquake.usgs.gov/data/slab/, are indicated in kilometres. The map also illustrates the locations of active volcanoes during the Holocene, the location of the buoyant Nazca ridge plus patterns of earthquake occurrence. Interestingly, basins with fast and slow denudation rates are situated in all litho-tectonic and geodynamic positions. This implies that tectonic processes do not exert a strong control on the denudation rate pattern. The purple strip east of the trench axis corresponds to the swath over which the historical earthquake data, presented in Figure 3, have been presented. The thick brown line delineates the swath over which elevation data of the coastal segment are displaced in Figure 3 [Colour figure can be viewed at wileyonlinelibrary.com]
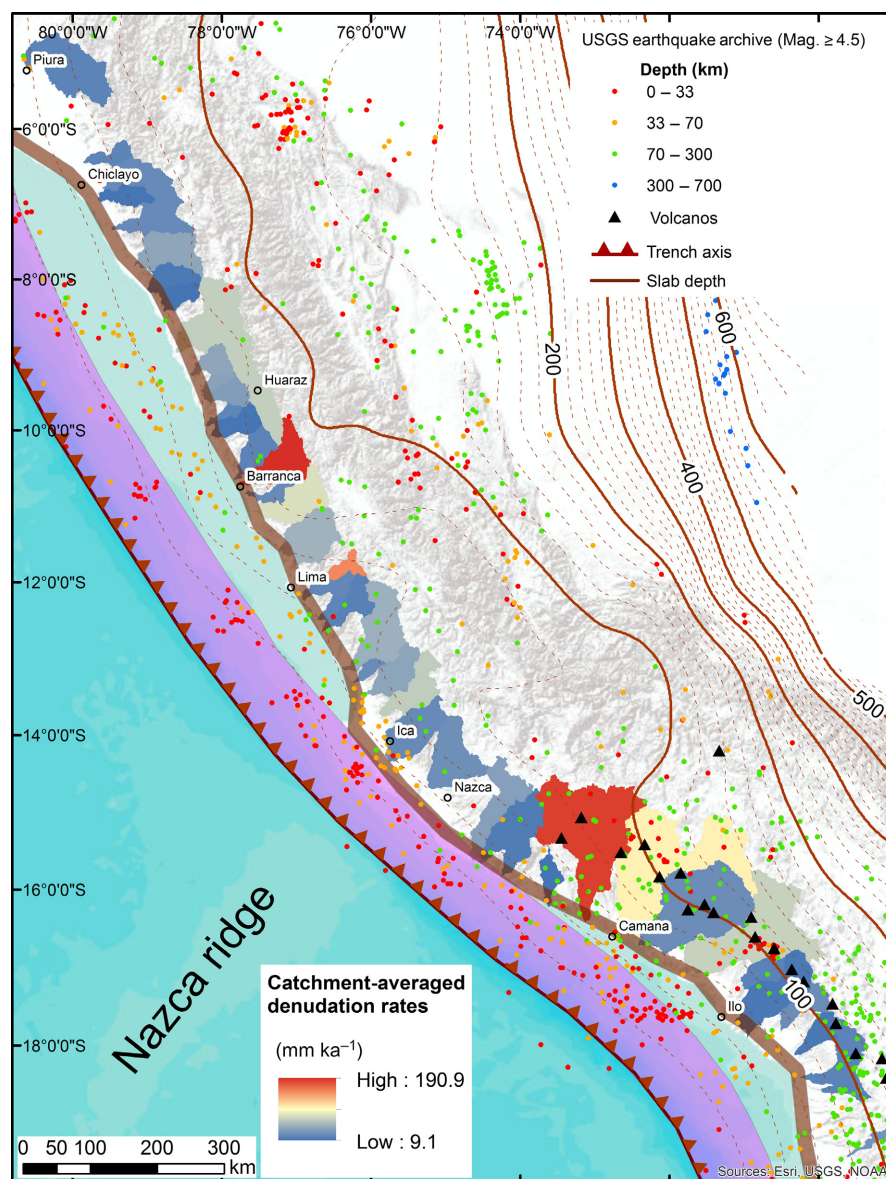
4 | RESULTS

Concentrations of in situ produced ^{10}Be in the quartz fraction of river sediments range from 6×10^4 to 1×10^6 at. g^{-1}, with most sites yielding values of *c.* 4×10^5 at. g^{-1}. The highest concentration of ^{10}Be was measured for the Quebrada Arunta (18.1°S latitude), while the lowest one was encountered for the Pativilca River at 10.7°S latitude (Table 2). The ^{10}Be concentrations result in basin-averaged denudation rates that range between 10 mm ka^{-1} and 260 mm ka^{-1} (Table 2). Basins located in northern Peru and northern Chile yielded the lowest values, with denudation rates ranging from *c.* 40 mm ka^{-1} to 10 mm

ka^{-1}. Denudation-rate estimates that were corrected for differences in the relative quartz contents of the bedrock are 30% lower and range from 9 to 190 mm ka^{-1} (Table 2, Figures 2 and 3e), albeit with a similar spatial distribution to the non-corrected ones (Table 2). Note that the lower rates result from low ^{10}Be production rates for the coastal batholith, which has relatively high quartz contents, but is situated at lower elevations. We will use these latter rates, which we have corrected for differences in quartz contents, in the following analysis.

A closer inspection of the denudation-rate pattern shows that the corresponding values are independent of the basins' seismotectonic situation. In particular, the coastal segment south of 13°S and
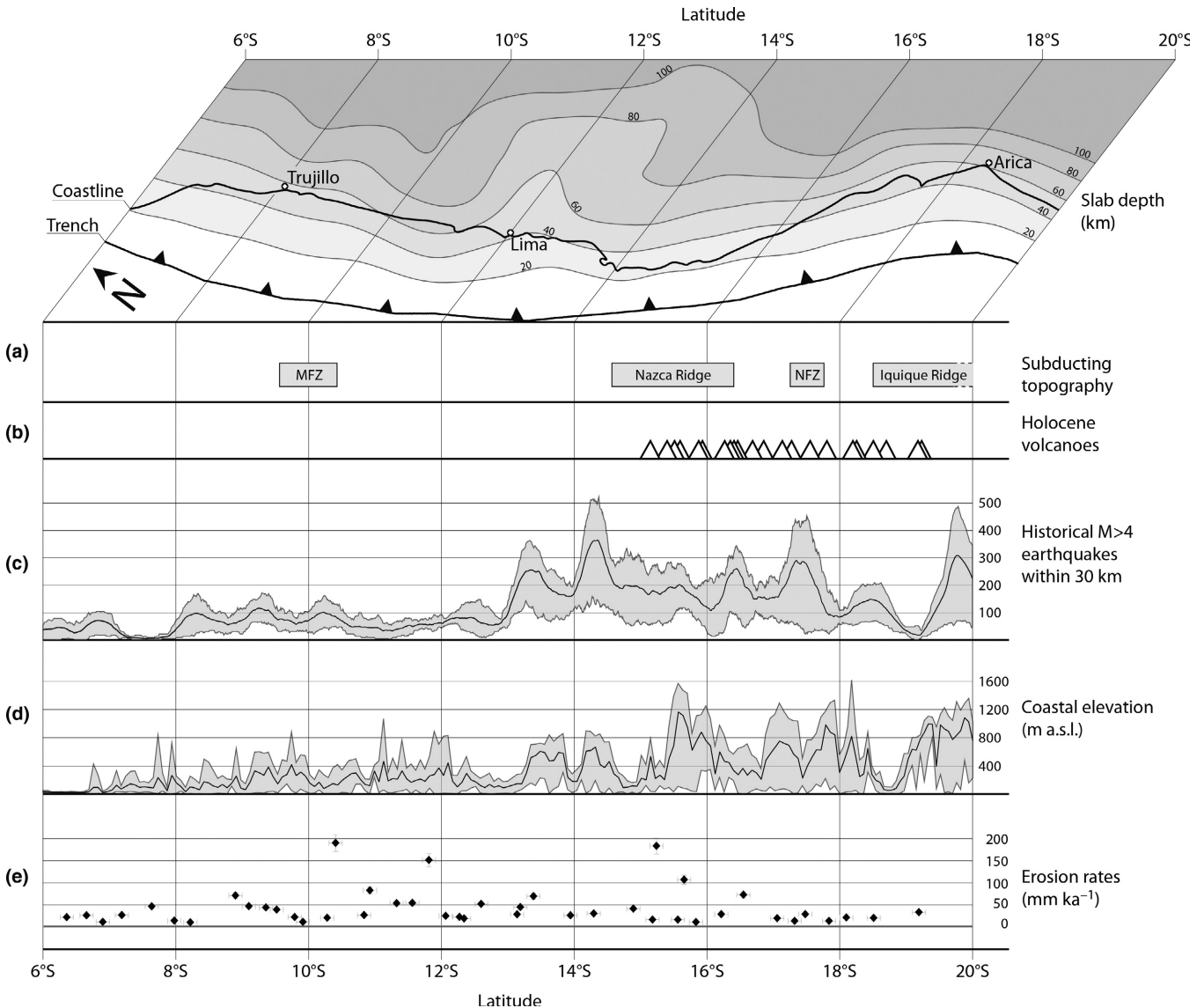
FIGURE 3 Topography of the subducting Nazca plate, where slab-depth data have been extracted from earthquake.usgs.gov/data/slab/. This N–S projection also illustrates (a) tectonic lineaments such as submarine ridges and fracture zones—MFZ: Mendaña Fracture Zone; NFZ: Nazca Fracture Zone; (b) Holocene volcanoes; (c) earthquake data, taken from earthquake.usgs.gov/earthquakes/search/; number of earthquakes *M* > 4 within a 30-km radius window; the 100-km wide swath along which earthquake data have been sampled is illustrated in Figure 2 as a purple strip adjacent to the trench; (d) coastal elevation; the data have been extracted from a 20-km wide swath profile along the coast; the sampling window is illustrated by a thick brown line in Figure 2; the three lines represent maximum, mean and minimum elevations within the selected swath; (e) catchment-averaged denudation rates have been corrected for quartz contents (Table 2). The latitudes represent the centroids of the basins (Table 1), which might deviate from the locations of the sample sites
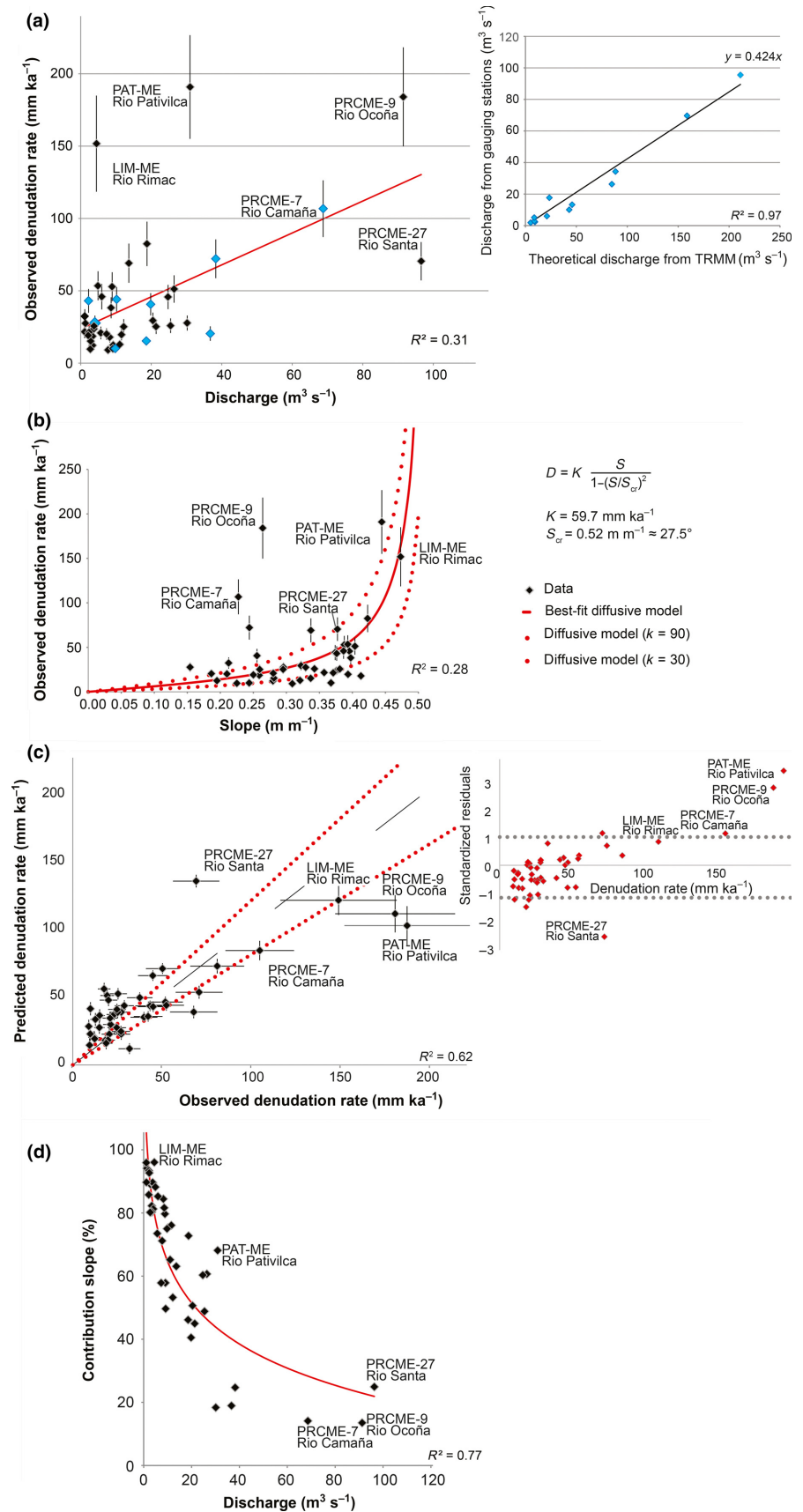
FIGURE 4 (a) Basin-averaged denudation rates plotted against mean annual discharge. The blue dots correspond to the data represented in the inset, showing the correlation between the mean annual discharge recorded by the gauging stations of the Peruvian hydrological survey and the theoretical discharge estimated from the TRMM database. (b) Denudation rates plotted against mean basin topographic gradients. The dashed red curves represent predictions for K values of 30 mm ka^{-1} and 90 mm ka^{-1}, with critical slopes of 0.52, which corresponds to 27.5°. (c) Plot showing predicted versus observed denudation rates using the empirical bilinear regression model and best-fit solutions for K^{*} and F coefficients of 42.6 ± 5.6 mm ka^{-1} and 1.1 ± 0.2, respectively. Dashed black line represents the 1:1 relationship, and red lines represent ±20% envelope around such an idealized model. The inset shows the standardized residuals from the model predictions plotted as a function of the observed denudation rates. (d) Estimated contribution of the slope component to the predicted denudation rates plotted as a function of the mean annual discharge [Colour figure can be viewed at wileyonlinelibrary.com]

particularly 16°S, where raised Quaternary marine terraces (Regard et al., 2010) suggest the occurrence of surface uplift, does not necessarily correspond with the region where denudation rates are highest (Figure 3), because values as high as 190 mm ka^{-1} are also encountered farther north where the coastal plain has been subsiding (Hampel, 2002). Likewise, segments where the Nazca plate subducts at a shallow angle and where the current seismicity implies a low degree of interseismic coupling (between 4°S and 17°S latitudes; Nocquet et al., 2014) do not correlate with a distinct denudation rate pattern either (Figure 3). Finally, there is no obvious correlation between the denudation rates and the pattern of earthquake frequencies (Figure 3c).

Positive correlations, albeit with a rather weak correlation coefficient (Pearson correlation coefficient *c.* 0.3, R^2 = 0.096, Table 4), exist between denudation and catchment-averaged hillslope angles. Likewise, denudation rates and mean annual discharge are positively linked (Table 4, Figure 4a). However, the relationships between denudation and mean basin slope are better explained by a non-linear diffusive mass transport model (Fig. 4b; e.g., Roering, Kirchner, & Dietrich, 1999):

$$D = K \frac{S}{1 - (S/S_{cr})^2}, \tag{1}$$

where denudation rate D is proportional to mean basin slope S for low gradients, while these relationships become non-linear for slopes approaching a critical value S_{cr}, which in our case equals 27.5°. Here, K represents the transport coefficient (Figure 4b).

Because the results of the Pearson correlation coefficient analysis reveal that runoff and mean basin slope are independent (Table 4), we additionally explored whether an empirical bilinear regression model is capable of explaining the spatial distribution of denudation rates along the western margin of the Peruvian Andes. This model considers runoff and slope as variables and has the form:

$$D = K^* S^* + FR \tag{2}$$

where denudation rate D is predicted as a function of mean basin slope $S^* = S/(1 - (S/S_{cr})^2)$ according to equation 1 and water discharge R. Here, K^* and F correspond to transport coefficients. The best-fit model solution, explaining >60% of the observed denudation rates (Figure 4c) at $p < 0.0001$, yields additional information on the positive correlations between denudation, mean basin slope and mean annual discharge. In particular, slope exerts an important control on denudation in those basins where mean annual discharge is low. Contrariwise, discharge becomes a relatively stronger control on denudation in basins where hillslopes are shallow (Figure 4d).

5 | DISCUSSION AND CONCLUSION

It has been proposed that erosion along the western Andean margin is strongly controlled by the seismicity pattern (McPhillips et al., 2014). Although earthquakes in combination with strong rainfall events (Bekaddour et al., 2014) are likely to release large volumes of debris flows and landslides in individual basins such as in the Pisco valley (McPhillips et al., 2014), we disregard tectonic processes as the

primary driving force on denudation at the scale of the western margin of the Peruvian Andes, at least for timescales spanning millennia. Indeed, south of 13°S latitude, the relatively high frequency of earthquakes and the raised Quaternary marine terraces point towards a strong tectonic driving force at work, which in turn is expected to promote erosion (Figure 3). Such a relationship, however, cannot be detected in our dataset as the denudation rate pattern is identical north and south of 13°S. Instead, we use the positive correlations between ^{10}Be-based basin-averaged denudation rate, mean basin slope and mean annual discharge to invoke an environmental control on denudation over ^{10}Be time-scales spanning millennia. In addition, the correlation pattern outlined in Figure 4d reveals that fast denudation has preferentially been promoted in basins where either slopes are steep or mean annual discharge has been large. Our interpretation about an environmental control is consistent with the results of morphometric analyses conducted over the entire western Andean margin, where erosion indices correlate positively with variables indicative of climate regimes (Montgomery, Balco, & Willett, 2001). Similarly, for the Andean margin south of 27°S, where climate shifts from arid to semi-humid, Carretier et al. (2013) reported slope and climate variability as primary controls on ^{10}Be-based denudation. Note that our precipitation data are too sparse to explore whether rainfall variability may also exert a measurable control on denudation in Peru, but we consider it very likely that positive correlations between these variables do exist. Finally, basins with higher-than-predicted denudation rates (Rio Ocoña and Pativilca; Figure 4c) show glacier remnants and glaciogenic-material accumulations in their headwaters that might supply ^{10}Be-depleted sediments to the river load, and could yield, in turn, overestimated denudation estimates (Delunel, van der Beek, Bourlès, Carcaillet, & Schlunegger, 2014). Contrariwise, Rio Santa's denudation rate appears lower than predicted (Figure 4c), possibly due to the presence of sedimentary basins at the foothill of the Cordillera Blanca (Margirier et al., 2015) that could act as a sediment trap, thereby decoupling the basin's sediment and water budgets and yielding an overestimated model prediction of the denudation.

In conclusion, neither flat-slab subduction nor along-strike differences in the seismic coupling between the Nazca and South American plates (Nocquet et al., 2014) appear to have exerted a measurable control on the denudation rate pattern at the basin scale along the western margin of the Peruvian Andes. Instead, a combination of runoff and mean basin slope appears to explain >60% of the denudation rate data, thus pointing to a strong environmental control on the erosional pattern in this part of the Andes. Similar relationships have been found for Northern Chile at *c.* 18°S where the climate is hyperarid (Kober et al., 2009) and for the western Andean margin south of 27°S, where the climate turns wetter (Carretier et al., 2013). We do not exclude a tectonic forcing on the landscape form, as the initiation of headward-retreating knickzones and the establishment of high topographies were certainly driven by tectonic uplift (Schildgen et al., 2007). While these forces have to be considered for time-scales spanning some Ma, we propose that for shorter time intervals spanning some thousand years, erosion along the western Andean margin has primarily been controlled by climate variables.

REFERENCES

Abbühl, L. M., Norton, K. P., Jansen, J. D., Schlunegger, F., Aldahan, A., & Possnert, G. (2011). Erosion rates and mechanisms of knickzone retreat inferred from [10]Be measured across strong climate gradients on the northern and central Andes western escarpment. *Earth Surface Processes and Landforms*, 36, 1464–1473.

Abbühl, L., Norton, K. P., Schlunegger, F., Kracht, O., Aldahan, A., & Possnert, G. (2010). El Niño forcing on [10]Be-based surface denudation rates in northwestern Peruvian Andes? *Geomorphology*, 123, 257–268.

Akçar, N., Deline, P., Ivy-Ochs, S., Alfimov, V., Hajdas, I., Kubik, P. W., ... Schlüchter, C. (2012). The 1717 AD rock avalanche deposits in the upper Ferret Valley (Italy): A dating approach with cosmogenic [10]Be. *Journal of Quaternary Science*, 27, 383–392.

Barnes, J. B., & Ehlers, T. A. (2009). End member models for Andean Plateau uplift. *Earth Science Reviews*, 97, 105–132.

Bekaddour, T., Schlunegger, F., Vogel, H., Delunel, R., Norton, K. P., Akçar, N., & Kubik, P. (2014). Paleo erosion rates and climate shifts recorded by Quaternary cut-and-fill sequences in the Pisco valley, central Peru. *Earth and Planetary Science Letters*, 390, 103–115.

Braucher, R., Merchel, S., Borgomano, J., & Bourlès, D. L. (2011). Production of cosmogenic radionuclides at great depth: A multi element approach. *Earth and Planetary Science Letters*, 309(1), 1–9.

Carretier, S., Regard, V., Vassallo, R., Aguilar, G., Martinod, J., Riquelme, R., ... Guyot, J. L. (2013). Slope and climate variability control of erosion in the Andes of central Chile. *Geology*, 41(2), 195–198.

Carretier, S., Regard, V., Vassallo, R., Martinod, J., Christophoul, F., Gayer, E., ... Lagane, C. (2015). A note on [10]Be-derived mean erosion rates in catchments with heterogeneous lithology: Examples from the western Central Andes. *Earth Surface Processes and Landforms*, 40(13), 1719–1729.

Chmeleff, J., von Blanckenburg, F., Kossert, K., Gerstmann, U. C., Knie, K., Rugel., G., ... Remmert, A. (2010). Determination of the Be-10 half-life by multicollector ICP-MS and liquid scintillation counting. *Nuclear Instruments and Methods in Physics Research Section B*, 268, 192–199.

Delunel, R., van der Beek, P., Bourlès, D., Carcaillet, J., & Schlunegger, F. (2014). Transient sediment supply in a high-altitude Alpine environment evidenced through a 10Be budget of the Etages catchment (French Western Alps). *Earth Surface Processes and Landforms*, 39, 890–899.

Garreaud, R., Vuille, M., & Clement, A. C. (2003). The climate of the Altiplano: Observed current conditions and mechanisms of past changes. *Paleogeography, Paleoclimatology, Paleoecology*, 194, 5–22.

Hampel, A. (2002). The migration history of the Nazca Ridge along the Peruvian active margin: A re-evaluation. *Earth and Planetary Science Letters*, 203(2), 665–679.

Huffman, G. J., Adler, R. F., Bolvin, D. T., Gu, G., Nelkin, E. J., Bowman, K. P., ... Wolff, D. B. (2007). The TRMM multi-satellite precipitation analysis: Quasi-global, multi-year, combined-sensor precipitation estimates at fine scale. *Journal of Hydrometeorology*, 8, 38–55.

INGEMMET (Instituto Geologico Minero y Metalurgico de Peru) (2011). *Geología Nacional. Geocatmin versión 1.5.1, Capa 12*. Lima, Peru: Instituto Geologico Minero y Metalurgico.

Isacks, B. L. (1988). Uplift of the Central Andean plateau and Bending of the Bolivian Orocline. *Journal of Geophysical Research*, 93(B4), 3211–3231.

Jarvis, A., Reuter, H. I., Nelson, A., & Guevara, E. (2008). Hole-filled SRTM for the globe Version 4. Retrieved from http://srtm.csi.cgiar.org (CGIAR-CSI SRTM 90 m Database).

Kober, F., Ivy-Ochs, S., Zeilinger, G., Schlunegger, F., Kubik, P. W., Baur, H., & Wieler, R. (2009). Complex multiple cosmogenic nuclide concentration and histories in the arid Rio Lluta catchment, northern Chile. *Earth Surface Processes and Landforms*, 34, 398–412.

Korschinek, G., Bergmaier, A., Faestermann, T., Gerstmann, U. C., Knie, K., Rugel, G., ... Remmert, A. (2010). A new value for the half-life of Be-10 by heavy-ion elastic recoil detection and liquid scintillation counting. *Nuclear Instruments and Methods in Physics Research Section B: Beam Interactions with Materials and Atoms*, 268, 187–191.

Kubik, P. W., & Christl, M. (2010). [10]Be and [26]Al measurements at the Zurich 6 MV Tandem AMS facility. *Nuclear Instruments and Methods in Physics Research Section B: Beam Interactions with Materials and Atoms*, 268, 880–883.

Margirier, A., Robert, X., Audin, L., Gautheron, C., Bernet, M., Hall, S., & Simon-Labric, T. (2015). Slab flattening, magmatism, and surface uplift in the Cordillera Occidental (northern Peru). *Geology*, 43(11), 1031–1034.

McPhillips, D., Bierman, P. R., & Rood, D. H. (2014). Millennial-scale record of landslides in the Andes consistent with earthquake trigger. *Nature Geoscience*, 7(12), 925–930.

Montgomery, D. R., Balco, G., & Willett, S. D. (2001). Climate, tectonics, and the morphology of the Andes. *Geology*, 29(7), 579–582.

Mudd, S. M., Harel, M. A., Hurst, M. D., Grieve, S. W. D., & Marrero, S. M. (2016). The CAIRN method: Automated, reproducible calculation of catchment-averaged denudation rates from cosmogenic radionuclide concentrations. *Earth Surface Dynamics*, 4, 655–674.

Nocquet, J. M., Villegas-Lanza, J. C., Chlieh, M., Mothes, P. A., Rolandone, F., Jarrin, P., ... Martin, X. (2014). Motion of continental slivers and creeping subduction in the northern Andes. *Nature Geoscience*, 7(4), 287–291.

Regard, V., Saillard, M., Martinod, J., Audin, L., Carretier, S., Pedoja, K., ... Hérail, G. (2010). Renewed uplift of the Central Andes Forearc revealed by coastal evolution during the Quaternary. *Earth and Planetary Science Letters*, 297(1), 199–210.

Roering, J. J., Kirchner, J. W., & Dietrich, W. E. (1999). Evidence for non-linear, diffusive sediment transport on hillslopes and implications for landscape morphology. *Water Resources Research*, 35(3), 853–870.

Schildgen, T. F., Hodges, K. V., Whipple, K. W., Reiners, P. W., & Pringle, M. S. (2007). Uplift of the western margin of the Andean Plateau revealed from canyon incision history, southern Peru. *Geology*, 35, 523–526.

SERNAGEOMIN (Servicio Nacional de Geología y Minería). (2004). *Mapa Geológico de Chile: Versión digital*. Servicio Nacional de Geología y Minería, Publicación Geológica Digital No. 7 (versión 1.0). Santiago, Chile: Servicio Nacional de Geología y Minería.

Thouret, J. C., Wörner, G., Gunnell, Y., Singer, B., Zhang, X., & Souriot, T. (2007). Geochronologic and stratigraphic constraints on canyon incision and Miocene uplift of the Central Andes in Peru. *Earth and Planetary Science Letters*, 263(3), 151–166.

Vidal, J. C. (1993). *Geología de los cuadrangulos de Huambo y Oropampa. Boletin, Serie A: Carta Geológica Nacional, no. 46*. Lima: Instituto Geológico Minero y Metalurgico.